



Frustrated peptide chains at the fibril tip control the kinetics of growth of amyloid- β fibrils

Yuechuan Xu^{a,1}, Kaitlin Knapp^{b,c,1}, Kyle N. Le^{b,d}, Nicholas P. Schafer^{b,c}, Mohammad S. Safari^{a,e}, Aram Davtyan^c, Peter G. Wolynes^{b,c,2}, and Peter G. Vekilov^{a,f,2}

^aWilliam A. Brookshire Department of Chemical and Biomolecular Engineering, University of Houston, Houston, TX 77204-4004; ^bCenter for Theoretical Biological Physics, Rice University, Houston, TX 77251-1892; ^cDepartment of Chemistry, Rice University, Houston, TX 77251-1892; ^dDepartment of Mechanical Engineering, University of Houston, Houston, TX 77204-4006; ^eDepartment of Molecular Biology, Princeton University, Princeton, NJ 08544-1014; and ^fDepartment of Chemistry, University of Houston, Houston, TX 77204-5003

Edited by Lia Addadi, Weizmann Institute of Science, Rehovot, Israel, and approved August 10, 2021 (received for review June 25, 2021)

Amyloid fibrillization is an exceedingly complex process in which incoming peptide chains bind to the fibril while concertedly folding. The coupling between folding and binding is not fully understood. We explore the molecular pathways of association of A β 40 monomers to fibril tips by combining time-resolved in situ scanning probe microscopy with molecular modeling. The comparison between experimental and simulation results shows that a complex supported by nonnative contacts is present in the equilibrium structure of the fibril tip and impedes fibril growth in a supersaturated solution. The unraveling of this frustrated state determines the rate of fibril growth. The kinetics of growth of freshly cut fibrils, in which the bulk fibril structure persists at the tip, complemented by molecular simulations, indicate that this frustrated complex comprises three or four monomers in nonnative conformations and likely is contained on the top of a single stack of peptide chains in the fibril structure. This pathway of fibril growth strongly deviates from the common view that the conformational transformation of each captured peptide chain is templated by the previously arrived peptide. The insights into the ensemble structure of the frustrated complex may guide the search for suppressors of A β fibrillization. The uncovered dynamics of coupled structuring and assembly during fibril growth are more complex than during the folding of most globular proteins, as they involve the collective motions of several peptide chains that are not guided by a funneled energy landscape.

amyloid fibrillization | fibril growth | frustrated states | Alzheimer's

The formation of amyloid fibrils of various proteins is a cardinal characteristic of several neurodegenerative diseases that afflict the growing aging populations worldwide (1, 2). Alzheimer's patients display neurofibrillary tangles made up of tau protein and accumulate plaques of the protein fragment amyloid- β (A β) outside neurons in the brain (3–6). The precise mechanism of pathogenesis remains unclear. According to one view, neurotoxic A β oligomers are the culprits (7–9), but much attention has focused on the structures and formation mechanisms of the A β fibrils and plaques, which are the most-characteristic disease markers (10–15). Notably, abundant plaque formation by the A β peptide mutated at positions Glu-22 (associated with the Dutch and Arctic types), Asp-23 (Iowa type), Leu-34 (Piedmont type), and others has been found to cause severe cerebral amyloid angiopathy (16). Cleaving the amyloid precursor protein generates a population of different-length polypeptide chains (17, 18). Two A β peptide isoforms, composed of 40 or 42 amino acid residues, A β 40 and A β 42, are the dominant components of fibrils in vivo (11, 19, 20). Here, we focus on the shorter peptide, A β 40, which is present at 5- to 10-fold-higher concentrations than A β 42 (21) and is overrepresented in mature fibrils and plaques (22, 23).

The assembly of A β peptides into fibrils is exceedingly complex (24). After the peptides diffuse toward each other, they establish contacts between their amino acid residues and realign these contacts to find conformations that minimize the free energy of the emerging structure (25). The first stage of this process, referred to

as nucleation, engenders a population of small oligomers that may themselves be pathogenic (25–28). Nucleation is succeeded by growth, in which peptides remaining in solution associate with the existing fibrils (29–31). After further growth, the longer fibrils may fracture, doubling the number of growing tips and releasing peptide oligomers, which in turn boost nucleation (28, 32). The fibrils also can branch by secondary nucleation. Both processes autocatalytically accelerate fibrillization (33). This complex series of events can lead to explosive growth of both oligomers and fibrils and encourage the spread of the aggregates and disease in patients' brains.

The entangled fibrillization processes are typically studied in bulk assays (28, 33–35), which often employ agents such as Thioflavin T (35) that fluoresce at a specific wavelength when bound to an amyloid structure (36). The fluorescence signal is assumed to scale with the total fibril mass, which increases due to fibril nucleation, growth, fragmentation, and branching occurring in parallel (37). The presence of a fluorescent tag that binds to the fibrils, however, may modify the kinetics. In bulk assays, the contributions of each of the constituent processes to the evolution of the signals cannot be directly evaluated but must be assessed from fits to models in which each step is expected to obey simple kinetic laws (28, 33, 35). Usually, fibril growth has been approximated as a simple bimolecular reaction between the fibril tips and solute peptides (28, 31). Recent studies have employed atomic force microscopy (AFM) (37–44) and fluorescence microscopy (45–49) to monitor the growth of individual amyloid fibrils of diverse proteins and peptides. In contrast with the steady bimolecular reaction at the fibril tips, usually assumed

Significance

Amyloid fibril growth is a probable key step in Alzheimer's disease pathogenesis, and growing fibril tips may represent the "Achilles' heel" of the process. We combine thermodynamic and kinetic experiments at the single-fibril level with molecular modeling, exclusively focused on events at the fibril tip. The experiments provide strong evidence for the role of frustrated intermediate states in fibrillization. The frustrated intermediates provide fresh targets in the search for potential drugs for Alzheimer's disease.

Author contributions: P.G.W. and P.G.V. designed research; Y.X., K.K., K.N.L., N.P.S., M.S.S., A.D., and P.G.V. performed research; Y.X., K.K., P.G.W., and P.G.V. analyzed data; Y.X., K.K., P.G.W., and P.G.V. wrote the paper.

The authors declare no competing interest.

This article is a PNAS Direct Submission.

Published under the PNAS license.

¹Y.X. and K.K. contributed equally to this work.

²To whom correspondence may be addressed. Email: vekilov@uh.edu or pwolynes@rice.edu.

This article contains supporting information online at <https://www.pnas.org/lookup/suppl/doi:10.1073/pnas.2110995118/-DCSupplemental>.

Published September 13, 2021.

in the models of bulk fibrillization, the growth trajectories sometimes incorporate periods of complete stagnation and the two ends of a fibril often grow at distinct rates. Asymmetric, unsteady, stagnant, and nonbimolecular fibril growth modes have not been considered in the current models. In consequence, the molecular mechanisms of fibril growth have remained elusive, severely restraining the search for ways to suppress amyloid fibrillization.

In the studies reported here, we synergistically join experiments with simulations. We examine the mechanisms of A β fibril growth by monitoring individual fibrils (50). Of the two reagents in the bimolecular reaction between fibril tips and the dissolved peptides that leads to fibril growth, the fibril tips are at a concentration lower by orders of magnitude than the peptide concentration. Hence, insight into the structures and dynamics of the fibril tips may potentially provide a route to block fibrillization by agents operational at substantially lower concentrations than those needed to suppress other stages of fibrillization. Our most-powerful tools are the correlations between the measured growth rates, peptide concentration in the solution, and the effect of denaturant, which directly illuminate the mechanism of peptide incorporation and can be compared quantitatively to computer simulations. For insights on the energetics of the intermediate and transition states for fibril incorporation, we study the effect of added urea, whose impact on the formation of interchain and intrachain contacts is relatively well understood from studies of protein folding. The direct determination of individual fibril growth rate that we employ affords the opportunity to elucidate the mechanistic complexity arising from the concurrent binding and folding of the incoming peptide chains.

Results and Discussion

Kinetics of Fibril Growth. To examine the growth of A β 40 fibrils, we use time-resolved in situ AFM (Fig. 1 and *SI Appendix, Fig. S1*) (50). We deposit fibril seeds on mica and monitor the growth of both fibril ends toward fixed reference points (Fig. 1*A*) in solutions of A β 40 monomer (*SI Appendix, Fig. S2*) with known concentrations. We evaluate the fibril growth rate as the slope of the time correlation of the fibril tip displacement (Fig. 1*E*) (50). Our previous work employing this method (50) revealed that the fibril growth rates and solubility measured using in situ AFM are close to those determined from time-dependent bulk growth of fibrils in solution (31). This comparison certifies that interactions with the substrate that may strain the fibrils or assist the supply of monomers to the fibril tip do not modify the growth rates, in contradistinction to results with A β 42, the short amyloid peptide A β (12–28), and amylin (43, 51, 52). We also established that the opposite ends of individual fibrils grow at similar rates, and the growth was relatively steady (50). Time-resolved in situ AFM monitoring of fibril growth revealed that the fibrils readily dissolved in quiescent peptide-free solutions (Fig. 1*B* and *F*).

The addition of urea led to significant increase of the fibril solubility: the fibrils dissolved at concentrations at which they otherwise grew in urea-free solutions (Fig. 1*C*). Urea-induced thermodynamic fibril destabilization, manifested as higher solubility, is consistent with urea's known activity as a universal protein denaturant (53) owing to its favorable interaction with the amide groups of the peptide backbones (54). This interaction impairs not only the formation of contacts between segments of a single chain that support folded protein structures but also the formation of contacts between distinct chains within amyloid fibrils (55). Increasing the peptide concentration in the presence of urea, however, leads to growth rates significantly faster than the values recorded at the same peptide concentration in the absence of urea (Fig. 1*D*). The acceleration of fibril growth in the presence of urea would appear contrary to the destabilization of the contacts that support the fibril structure (56, 57).

The correlation between the fibril growth rate R and the A β 40 concentration C is linear (Fig. 2*A*). The observed linearity

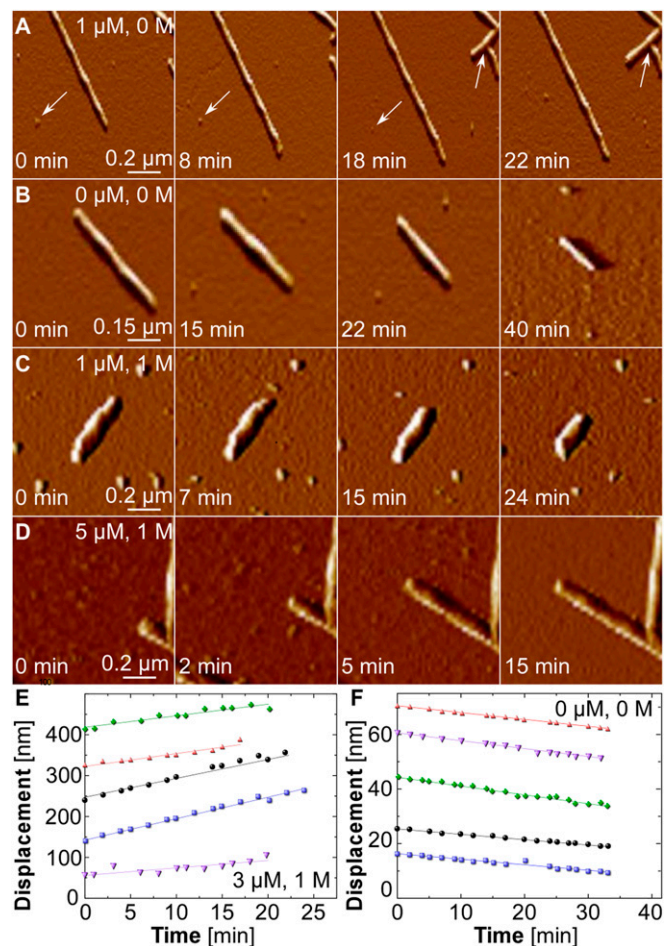


Fig. 1. Growth and dissolution of A β 40 fibrils. (A–D) Time-resolved in situ AFM monitoring of the evolution of growth and dissolution of A β 40 fibrils at different concentrations of A β 40 in μ M and urea in M. The arrows in A point to immobile objects used as reference to measure the displacement of fibril tips. (E and F) Evolutions of the displacements of 10 fibril ends. The straight lines represent best fits that were used to determine the fibril growth rates. (E) Fibril growth at A β 40 solution concentration 3 μ M in the presence of 1 M urea. (F) Fibril dissolution in peptide-free and urea-free buffer.

implies that the fibrils grow by association of the dominant solution A β 40 species, whether it be monomer, dimer, or a heavier oligomer (58). Whereas oligomers of varying compositions are present in A β solutions, they reside in equilibrium with the monomers, which capture the majority of the peptide mass in the solution (59, 60). Growth by association of oligomers in equilibrium with a majority of monomers would manifest as a superlinear (e.g., quadratic, for growth by dimer association) $R(C)$ correlation (58). We tentatively conclude that A β 40 fibrils grow by association of monomers.

The $R(C)$ correlation crosses the interpolated line of zero growth at $C_e = 0.44 \pm 0.07 \mu$ M (50). For C below C_e , the negative values of R correspond to fibril dissolution (Figs. 1*B* and 2*A*). A solution with concentration C_e is in equilibrium with the fibrils (i.e., C_e is the A β 40 solubility with respect to the fibrils). The equilibrium $F_n + M \rightleftharpoons F_{n+1}$, where F_n and F_{n+1} denote fibrils that differ in length by one monomer M , is characterized by a constant $K = [M]_e^{-1}$, since the addition of a monomer does not modify the fibril concentration and $[F_n] = [F_{n+1}]$. Considering the dominance of monomers in the solution, we approximate the equilibrium monomer concentration $[M]_e$ with the total peptide concentration C_e at equilibrium with the fibrils and arrive at $K = C_e^{-1}$.

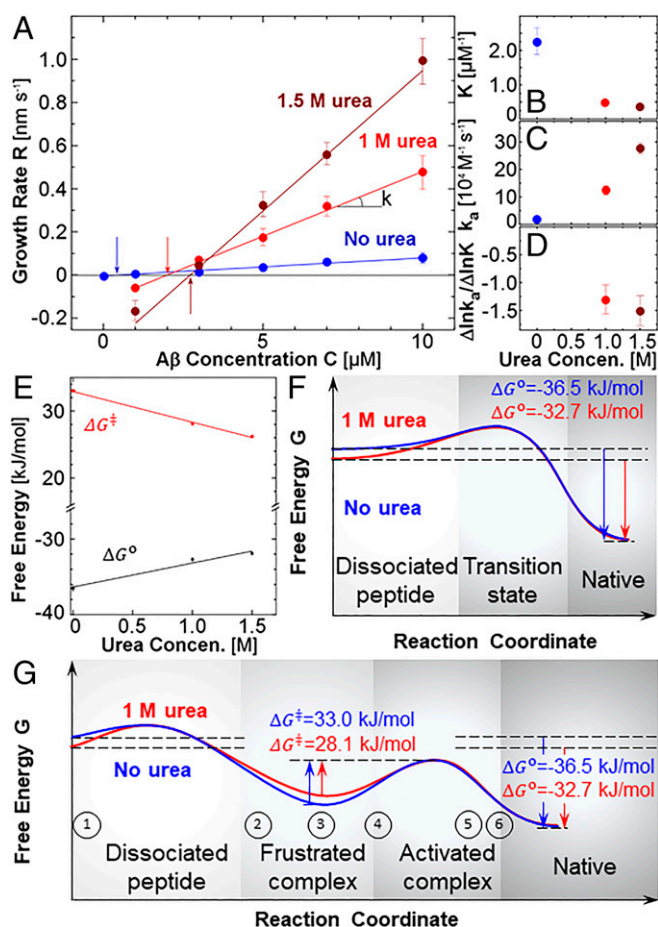


Fig. 2. The kinetics of Aβ40 fibril growth. (A) The dependences of the growth rates R of individual fibrils on the concentration C of Aβ40 in the absence and the presence of urea at two concentrations. The error bars correspond to the SD from the mean for 20 to 50 measurements illustrated in Fig. 1 E and F. The arrows mark the respective solubilities C_e . The rate constants k_a are determined from the slopes of the linear correlations. Data in the absence of urea are from ref. 50. (B and C) The equilibrium constant $K = C_e^{-1}$ in B and the rate constant k_a , in C for fibrillization in the absence and presence of urea at two concentrations determined from the $R(C)$ correlations in A. (D) The ratio $\Delta \ln k_a / \Delta \ln K$, evaluated from the data in B and C. The error bars in B–D indicate SDs from the mean values evaluated from the $R(C)$ correlations in A. (E) The correlations of the free energies for fibrillization ΔG° and of the transition state for incorporation ΔG^\ddagger with the urea concentration. The error bars indicate the SDs of ΔG° and ΔG^\ddagger and are smaller than the symbol size for most data points. (F) Schematic of the free energy landscape along a direct pathway of incorporation of a peptide chain into a fibril tip that does not involve any intermediate states. (G) Schematic of the free energy landscape along a pathway of incorporation of a peptide chain into a fibril tip that passes through a frustrated intermediate state. The encircled numbers denote approximate locations along the reaction coordinate of the conformations depicted in Fig. 3A. In F and G, blue curves and blue ΔG^\ddagger and ΔG° values characterize association to fibrils in the absence of urea, red curves and red ΔG^\ddagger and ΔG° values, in the presence of 1 M urea.

For insight into the mechanisms that guide faster growth in the presence of urea despite the fibril destabilization that this denaturant enforces, we measured the $R(C)$ correlations at two concentrations of urea, 1 and 1.5 M, and compared them to $R(C)$ data in urea-free solutions (Fig. 2A). At the three tested compositions, fibrillization was reversible. The growth and dissolution dynamics revealed by AFM images (Fig. 1 C and D) and the $R(C)$ correlations (Fig. 2A) demonstrate that urea acts as an apparent catalyst for growth and dissolution. It leads to both

faster fibril growth and faster dissolution (Fig. 2A), while increasing the Aβ40 solubility with respect to the fibrils.

The solubility boosts with added urea define gains of standard free energy of fibrillization, $\Delta G^\circ = -RT \ln K = RT \ln C_e$, from $-36.5 \pm 0.4 \text{ kJ} \cdot \text{mol}^{-1}$ in the absence of urea to $-32.7 \pm 0.3 \text{ kJ} \cdot \text{mol}^{-1}$ at 1 M urea and $-31.9 \pm 0.2 \text{ kJ} \cdot \text{mol}^{-1}$ at 1.5 M urea [i.e., about $3 \text{ kJ} \cdot \text{mol}^{-1}(\text{mole urea})^{-1}$ (Fig. 2E)]. The increasing ΔG° announces the expected urea-enforced destabilization of the fibrils relative to the solute monomers. We use fibril seeds that were generated without urea, and previous work has established that the structure of a fibril persists after the growth conditions deviate from those during fibril nucleation (11, 29, 61). The uniformity of the fibril structure during growth in the presence and absence of urea ascribes the destabilization of the fibrils relative to the solution to urea-imposed lower free energy of the solute peptide chains (Fig. 2 F and G).

We model the linear $R(C)$ correlation as $R = ak_a(C - C_e)$, where $a = 0.47 \text{ nm}$ is the contribution of an incorporated monomer to the protofilament length (29), and k_a is the bimolecular rate constant for the reaction between monomers and fibril tips. We define protofilament as a single stack of peptide chains (SI Appendix, Fig. S3) (62, 63); we discuss alternative definitions (29, 61, 64) in SI Appendix. The expression for R is akin to the result of a model, which assumes a two-step reaction of monomer association to the fibril tip, followed by incorporation into the fibril, under conditions where the first step is rate limiting (31). The constant k_a assumes values between 1.8×10^4 and $2.8 \times 10^5 \text{ M}^{-1} \cdot \text{s}^{-1}$, depending on the urea concentration (Fig. 2C). These values are significantly slower than the expected diffusion limit for association of about $10^{10} \text{ M}^{-1} \cdot \text{s}^{-1}$ (65). The rate constant can be written as $k_a = k_0 \exp(-\Delta G^\ddagger / k_B T)$, where k_B is the Boltzmann constant and T is temperature. We assume $k_0 = 10^{10} \text{ M}^{-1} \cdot \text{s}^{-1}$ as the diffusion limit (65). It has been argued that k_0 for Aβ40 fibril growth should be closer to $10^9 \text{ M}^{-1} \cdot \text{s}^{-1}$ (31); the exact value of k_0 , however, does not modify the arguments presented in *A Frustrated Complex at the Fibril Tip*. We assume that the rotational and orientational entropy contributions to k_0 are not substantially affected by urea. We note that urea increases the solution viscosity by 4% at 1 M and 6% at 1.5 M (66). Accounting for this increase would depress the values of G^\ddagger in the presence of urea by about $0.1 \text{ kJ} \cdot \text{mol}^{-1}$, which is within the experimental uncertainty of this variable (Fig. 2E). With this, the free energy barrier ΔG^\ddagger decreases from $33.0 \pm 0.1 \text{ kJ} \cdot \text{mol}^{-1}$ in the absence of urea to $28.1 \pm 0.2 \text{ kJ} \cdot \text{mol}^{-1}$ at 1.0 M urea and to $26.2 \pm 0.2 \text{ kJ} \cdot \text{mol}^{-1}$ at 1.5 M urea; that is, the barrier reduces by about $4 \text{ kJ} \cdot \text{mol}^{-1}(\text{mole urea})^{-1}$ (Fig. 2 E and G). Importantly, the correlation between ΔG^\ddagger and the urea concentration is linear (Fig. 2E). In analyses of protein folding kinetics, such linearity is taken as evidence that urea does not greatly modify the conformation of the transition state. In folding, observed kinetics nonlinearities have been shown to correlate to flatter free energy profiles with “malleable” transition states (67). The linearity here, while based on only three concentrations, suggests that lack of urea-enforced structure change in the transition state is a good first approximation.

A Frustrated Complex at the Fibril Tip. The opposing activation free energy ΔG^\ddagger and fibrillization free energy ΔG° responses to urea eliminate certain mechanisms of amyloid fibril growth that have previously been suggested based on simulations. One such proposal assumes that monomeric peptides undergo a conformational transformation into an aggregation-prone state, whose lifetime is longer than the time required for collision with a fibril tip (24). In this scenario, the depression of the free energy of the peptides in the solution enforced by urea would boost the free energy barrier for incorporation (Fig. 2F) and impose slower fibril growth, contrary to actual observations. From a broader perspective, the

opposing ΔG^\ddagger and ΔG^o trends defy any mechanism that constrains the urea impact to the peptide chains in the solution.

The essential identity of the bulk fibril structure in the presence and absence of urea eliminates urea-driven bulk fibril structure modifications as the mechanism that regulates the high sensitivity of ΔG^\ddagger to urea. The exclusion of peptides in the solution and fibril structure as targets for urea attack implies an incoming chain passes through an intermediate state, in which it attaches, but only partially, to the fibril tip. The substantial magnitude of ΔG^\ddagger and its sensitivity to urea together imply that the intermediate complex is bound by strong hydrophobic contacts, distinct from the native contacts that support the fibril structure and dictate ΔG^o . The unraveling of the initial nonnative contacts between the incoming and terminal fibril monomers, in search of the native conformation typical of the bulk fibril, becomes the rate-limiting step for the attachment of the monomer to the fibril tip and contributes to ΔG^\ddagger . The extension of the linear $R(C)$ correlation to dissolution in undersaturated solutions (Fig. 2A) indicates that disorder at the tip is an equilibrium feature of the fibril structure. Urea, by interacting with the backbones of monomers at the fibril tip (68, 69), weakens the nonnative contacts and thereby destabilizes the intermediate state, which lowers ΔG^\ddagger (Fig. 2G). Importantly, the linear correlation of ΔG^\ddagger with the urea concentration (Fig. 2E) indicates that the urea-induced weakening of the nonnative contacts likely stops short of modifying the structure of the intermediate and transition states. In protein folding, such energy-rich nonnative contacts have been called frustrated (70–72). Whereas simulations have foreseen frustrated states as amyloid peptides fold to incorporate into fibrils (25, 73, 74), the opposing ΔG^\ddagger and ΔG^o responses to urea, based on the divergent effects of urea on fibril solubility and growth rate, provide direct experimental evidence for the role of frustration in fibrillization.

The pathway of association of peptides with the fibril tips suggested by the rates of fibril growth (Fig. 2) shares certain features with a mechanism put forth by simulations. In this mechanism, the incorporation of a monomer into a fibril divides in two steps. First, the association of an unstructured monomer to the fibril tip (often called docking), followed by conformational rearrangement toward the peptide structure in the fibril bulk (locking) (24, 65, 75, 76). In the simplest lock-and-dock scenario, the conformational transformation of each captured peptide chain is templated by the previously arrived peptide. The magnitude of ΔG^\ddagger and the opposing ΔG^\ddagger and ΔG^o trends that we observe advocate a more complex picture whereby the docked state evolves to a frustrated complex, in which a monomer makes many nonnative contacts in the fibril tip.

Additional characteristics of the frustrated complex emerge when we quantitatively compare the urea-induced weakening of the frustrated contacts to what is seen for protein unfolding (77). Statistics over 45 proteins have revealed that urea-induced lowering of the free energy of unfolding scales with the protein surface area exposed to solvent upon unfolding (77). This proportionality indicates that the thermodynamic effect of urea of about $3 \text{ kJ} \cdot \text{mol}^{-1}$ (mole of urea) $^{-1}$ is associated with the loss of about $3,200 \text{ \AA}^2$ of solvent-accessible surface area (SASA) upon monomer incorporation into the fibril; we designate this loss as $\Delta \text{SASA}^0 = -3,200 \text{ \AA}^2$. The urea-induced activation free energy drop of about $4 \text{ kJ} \cdot \text{mol}^{-1}$ (mole of urea) $^{-1}$ corresponds to the exposure of $\Delta \text{SASA}^\ddagger = 5,300 \text{ \AA}^2$. The evaluations of ΔSASA^0 and $\Delta \text{SASA}^\ddagger$ afford the opportunity to compare the results of the kinetics experiments to those of simulations and thus attain additional insights in the incorporation pathway.

Interaction of the Monomer with the Fibril Tip during Binding and Folding. To achieve greater molecular-level understanding of how an incoming peptide chain acquires the structure typical of the fibril bulk as it incorporates into a fibril, we carried out simulations

using the associative memory, water-mediated structure, and energy model for molecular dynamics (AWSEM-MD) (78). The coarse-grained nature of the AWSEM simulation Hamiltonian leads to much more rapid sampling than models with explicit solvent molecules. Owing to the lack of solvent, 1 ps of simulation time compares to longer than a nanosecond of laboratory time. We used the Protein Database entry 2LMN, the polymorph examined with AFM (50), to construct the fibril structure. We evaluated the free energy profile for an incoming monomer to associate with a fibril composed of five chains arranged in a single stack (Fig. 3A). We characterized the conformational ensembles in terms of the distance between the center of mass of the peptide chain and the fibril end and by the similarity of the structure of the incoming monomer to that of a chain in the fibril bulk (Fig. 3B). We explored about 30 select configurations, divided into six groups, along the reaction pathway (Fig. 3A and B). We then computed the SASA of fully atomic models generated from the coarse-grained structures (Fig. 3C).

The computed change, $\Delta \text{SASA}_{\text{eq}} = \text{SASA}_6 - \text{SASA}_1$ (Fig. 3C), defines the sensitivity of the equilibrium ΔG^o to the addition of denaturant, and the model result $\Delta \text{SASA}_{\text{eq}} = 3,400 \text{ \AA}^2$ agrees

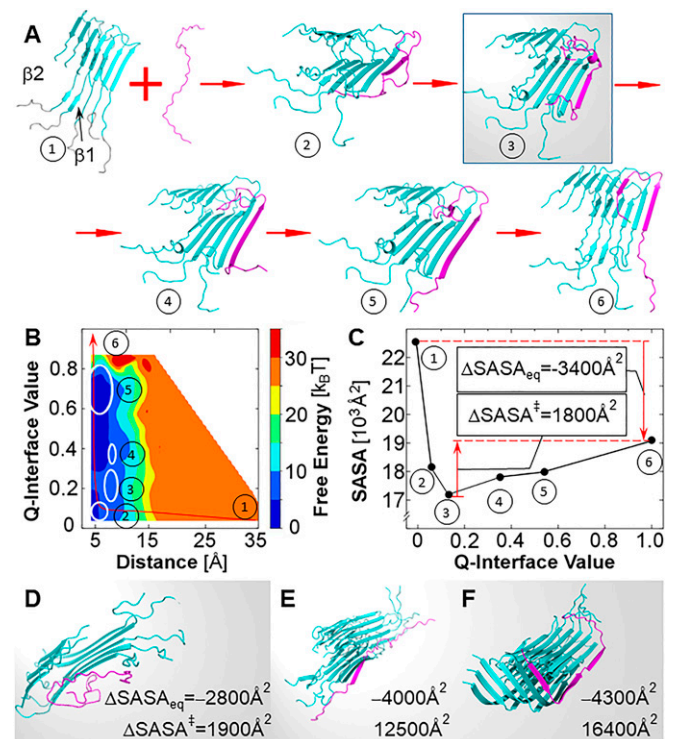


Fig. 3. Microscopic view of monomer association to a fibril tip. (A) Select successive conformations of a monomer peptide (magenta) associating to an even end (where the $\beta 1$ strand of a 2LMN protofibril is open) of a fibril comprised one protofibril (cyan), computed using AWSEM-MD simulations. 1, a dissociated peptide; 2 to 5, intermediate conformations; 6, peptide fully integrated in the fibril. (B) The free energy as a function of the distance from monomer end and Q-interface, which measures the similarity of the monomer structure to that in the fibril bulk. The white ovals next to 2 to 5 highlight pools of conformations, from which respective SASAs were sampled and averaged. The red arrow schematically depicts a reaction pathway. (C) Total SASA of the fibril and monomer in positions 1 to 6. Computed $\Delta \text{SASA}_{\text{eq}}$, corresponding to equilibrium, and $\Delta \text{SASA}^\ddagger$, representative of the activation barrier, are shown. (D–F) Conformations of a monomer peptide (magenta) associating with three different fibril tips (cyan) at which SASA is minimal, as conformation 3 in A. Listed negative areas represent $\Delta \text{SASA}_{\text{eq}}$ and positive areas, $\Delta \text{SASA}^\ddagger$. (D) The odd end of a 2LMN fibril comprised of one protofibril. (E) A fibril comprised of two protofibrils of equal length. (F) A fibril comprised of two protofibrils, of which one is longer by one monomer.

well with the estimate based on the measured urea dependence of the fibril solubility. The simulations reveal that the SASA passes through a minimum at position 3 (Fig. 3*A* and *C*). In this group of structures, an incoming monomer partially binds to itself forming nonnative inter- and intrachain contacts rather than forming native contacts with the fibril tip (Fig. 3*A* and *B*). These frustrated contacts must unravel as the peptide reconfigures to fully integrate into the fibril in the cluster 6 structures, labeled in Fig. 3*B*. Remarkably, the finding of an intermediate frustrated complex at the fibril tip agrees with the conclusions implied by the responses of experimentally measured ΔG^\ddagger and ΔG^o to added urea.

The positive Δ SASA between positions 3 and 6 represents only a rough estimate of the effects of urea on the activation free energy ΔG^\ddagger . All-atom simulations of the conformations of the peptides at the fibril tip yield Δ SASA $^\ddagger = 1,800 \text{ \AA}^2$. The results for monomer association to the opposite, odd, fibril end (Fig. 3*D* and *SI Appendix*, Fig. S5) are similar. Importantly, both values of Δ SASA ‡ are only about one-third of the value inferred from the response to urea of the growth kinetics of individual fibrils, measured by AFM. The discrepancy between the simulated and measured Δ SASA ‡ s suggests that the structure of the frustrated complex at the fibril tip is probably more elaborate than what has emerged from these initial simulations.

We envision two possible models of a more elaborate frustrated intermediate. First, the frustrated complex may involve more than one peptide chain within a single protofilament; the ratio between the experimental and simulated Δ SASA ‡ suggests that three or four monomers would need to be involved. Simulations of a peptide chain association with a disordered fibril tip would involve characterizing a multidimensional free energy landscape and require significant additional efforts. Alternatively, the intermediate frustrated state may involve binding of the incoming monomers to both protofilaments in a filament. The experimentally measured thicknesses of the fibrils monitored by AFM indicate that the majority of the filaments are built of two parallel protofilaments, represented by the 2LMN structure (50).

We explore the possibility where the incoming peptide chain associates to both protofilaments in a filament. We note that the addition of monomers to a double filament must ultimately preserve the structure of the twinned protofilaments, and this involves at least two alternating conformations of the fibril tip: one where the two protofilaments exactly match in length and one where one of the protofilaments is ahead by one monomer. AWSEM simulations of monomer attachment to the tip of a two-protofilament structure reveal that, instead of folding on top of one of the two monomers at the fibril tip, an incoming peptide chain spans both stacks and enforces a stabilized frustrated conformation that may be incapable of further growth (Fig. 3*E* and *F* and *SI Appendix*, Fig. S6). This state was predicted for both the matched and the mismatched protofilaments (Fig. 3*E* and *F*). Δ SASA ‡ from such frustrated states to the final conformation are greater than $12,000 \text{ \AA}^2$ (Fig. 3*E* and *F*).

The Growth of Fibrils with Bulk Structure of Their Tip. To discriminate experimentally whether the complex frustrated state at the fibril tip recruits more than one disordered peptide chain that crown a single protofilament or structures as a single chain that spans both protofilaments in a filament, we monitored the growth rates of freshly cut fibrils (Fig. 4*A*). In freshly cut fibrils, the peptides at the tip initially should carry the structure of monomers in the fibril bulk, and an intermediate state composed of more than one frustrated chains may not have had time to evolve. Thus, if the slow growth rate observed in the AFM experiments is due to a frustrated complex composed of several chains, freshly cut fibrils will grow faster than fibrils with normal tips. By contrast, if the high ΔG^\ddagger deduced from AFM experiments is due to interactions of a single incoming chain with two

adjacent protofilaments, the frustrated complex that crowns the freshly cut fibril tips will be identical to the one at equilibrated tips, and the freshly cut tips will grow with rates similar to those of normal tips.

The AFM measurements reveal that freshly cut fibrils initially grow about twice as fast as fibrils with equilibrated tips (Fig. 4*B* and *C*). In five of the cut fibrils, the growth rate transitioned to its “normal” value after 6 to 8 min, during which time the fibrils grew about 10 nm (Fig. 4*B*). The observed faster growth rates indicate that the freshly cut fibrils carry a simpler frustrated complex than equilibrated fibril tips. For a second test of the distinction between the kinetics of growth of freshly cut and mature fibrils, we measured the effects of 1 M urea on the growth of freshly cut fibrils and compare them to the growth rate of mature fibrils (Fig. 4*C*). The results reveal that urea accelerates the growth rate constant of freshly cut fibrils by about threefold, significantly weaker than its ca. sixfold effect on normal tips (Fig. 4*C*).

Collectively, the outcomes of the two tests with freshly cut fibrils indicate that the frustrated complex at equilibrated fibril tips comprises more than one peptide chain but is probably constrained to a single protofilament.

Conclusions

Time-resolved in situ AFM measurements of the growth kinetics of individual fibrils and molecular simulations suggest a two-step mechanism of growth of A β 40 fibrils, whereby an incoming monomeric solute peptide first associates to a complex residing at the fibril tip and composed of several other monomers that have nonnative conformations. The unraveling of the frustrated initial contacts during the conformational rearrangement of one of the constituent peptide to the bulk fibril structure constitutes the rate-limiting step for fibril assembly. The proposed reaction pathway should help guide the search for fibrillization inhibitors by finding small molecules that bind to the frustrated complex at the fibril tip and increase the free energy cost of rearranging it. In a broader context, our findings indicate that the coupled dynamics of structuring and assembly during fibril growth are more complex than observed for the folding of most globular proteins, since they involve the collective motions of several peptide

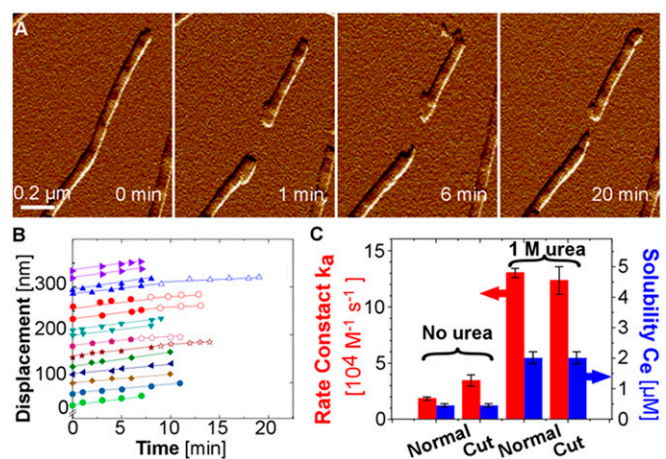


Fig. 4. The growth of fibrils with bulk structure of the peptides at the tip. (A) AFM micrographs of growth of freshly cut fibrils. (B) The displacement of the freshly cut ends. Five of the freshly cut tips transition to slower growth depicted with open symbols. (C) The rate constants k_a (red bars and *Left* axis) and the solubilities C_e (blue bars and *Right* axis) of fibrils with normal equilibrated tips and with freshly cut tips in the absence of urea and in the presence of 1 M urea. The error bars represent the SD from the mean evaluated from about 400 fibril tip displacement measurements for the normal fibrils and 100 fibril tip displacement measurements for the freshly cut as in Fig. 2 *A* and *C*.

chains that comprise the initial frustrated complex and simultaneously strain nonnative contacts in the transition state. Furthermore, the substantial kinetic consequences of this frustrated complex indicate that fibril growth does not enjoy a fully funneled energy landscape.

In the context of Alzheimer's disease, the low concentration of fibril tips in the fibrillization reaction mixture suggests that the tips may be suitable targets for attack by potential suppressors of fibrillization. The distinct structure of the fibril tip proposed here may guide the computational search for small molecule compounds and antibodies that bind to the tip and stunt fibril growth.

Materials and Methods

Detailed descriptions of all methods used in this work are provided in [SI Appendix](#).

Aβ40 Expression and Purification. We have expressed Aβ(M1-40) (MDAEFRHDSGYEVHHQKLVFFAEDVGSNKGAIIGLMVGGVVIA) in *E. coli* and purified it by size exclusion chromatography (50) following published procedures (79). This method produces Aβ peptide with a methionine attached to the N terminus ([SI Appendix, Fig. S2](#)), which significantly simplifies purification and contributes to several-fold-greater yields (79). The fibrillization kinetics of the methionine-initiated peptide quantitatively matches that of the methionine-free peptide (79), justifying the wide use of Aβ(M1-40) and Aβ(M1-42) in amyloid-β fibrillization studies (31, 35, 80).

Fibril Formation. Fibril seeds grew at 37 °C while stirred at 300 rpm on a table Inkubator 1000 (Heidolph) for 24 h. Seed generation in continuously stirred solutions enforces a twofold symmetric fibril structure, 2LMN (31, 50). The generation of fibril seeds was performed without any exposure to urea even for growth rate determinations in the presence of urea. In those latter runs, urea was added to the solution immediately before fibril growth observations with AFM.

Sample Preparation and In Situ AFM Imaging. We used a multimode atomic force microscope (Nanoscope VIII or IV, Bruker) for all AFM experiments. To prepare samples for growth rate measurements, aliquots of 2 μL second-generation fibril seeds was added to the incubation buffer; urea was added based on experiment needs. AFM images were collected in tapping mode.

The Growth of Freshly Cut Fibrils. Existing fibrils deposited on the AFM substrate were monitored under AFM for several minutes. To cut a fibril, we chose a relatively long one, which spanned about 50% of the image width. To ensure a good cut, we rotated the scan angle so that the angle between the fibril and fast scan direction angle was at least 45°. To increase the force of interaction between the tip and the fibril, we lowered the amplitude set point to 50 or 60% of the original value and set the scan frequency to 1 Hz to better control the length of the cut out. After the cut was complete, we reset the set point and the scan frequency to their original values to monitor the growth of the freshly cut ends.

Simulations. The simulations were carried out using the AWSEM force field (78). AWSEM represents proteins as coarse-grained structures, with every amino acid residue defined by the interactions of three beads: C_α, C_β, and O. The AWSEM Hamiltonian ensures an ideal backbone geometry between the explicit beads and includes terms accounting for secondary and tertiary interactions, implicit solvent effects, and residue burial preferences. To simulate the growth of an Aβ40 fibril, we used the structure of a twofold symmetric polymorph consisting of U-shaped protofilaments with a positive stagger (2LMN) (81). We chose this structure because it likely represents the polymorph that forms under the conditions employed in the AFM experiments (50).

To study the free energy associated with monomer addition, we introduce the order parameter Q-interface in the following form:

$$Q_{\text{interface}} = \frac{1}{N_p} \sum_{|i-j|>2} e^{-\left(\frac{r_{ij}-r_{ij}^N}{2\sigma_{ij}}\right)^2}$$

where r_{ij} is the interatomic distance between the C-α atoms of residues i and j , and r_{ij}^N is the distance between the same C-α atoms in the fully aligned fibril $n + 1$ structure. The term σ_{ij} defines the distribution width, which is minimally influenced by the sequence distance between the i and j C-α atoms. The value of Q-interface ranges from 0 (completely dissimilar contacts) to 1 (native contacts), as enforced by the normalization by N_p , the number of unique residue pairs that satisfy the $|i - j| > 2$ conditions.

Umbrella sampling simulations were performed with a biasing force between the center-of-mass of the free monomer and the center-of-mass of the chain sitting at the tip of the protofilament (65).

The set of simulations performed for modeling monomer additions at either end of the protofilament—to compare the dynamics of a positive and negative stagger—and across the full range of distance biasing and temperatures, resulted in trajectories totaling 0.46 μs. A timestep of 2 fs was used for all simulations, and each simulation ran for a total of 2,500,000 steps (5 ns), with the first 0.042 ns of each simulation disregarded to allow for equilibration. Potential of mean force plots were generated using the multistate Bennet acceptance ratio (82) to remove the biasing term contribution to the energy calculations from umbrella sampling (Fig. 3B).

To compare the simulations results with results of the fibril growth kinetics experiments, we evaluate degree of burial of sex distinct conformations along the reaction pathway in terms of the total SASA. Even though AWSEM represents each amino acid with three beads, which correspond to the C_α, C_β, and O atoms, it allows for the reconstruction of all heavy atoms of the backbone under the assumption of backbone planarity and ideal geometry. To perform the SASA calculations, the CG conformations were first back-mapped to all-atom representations using Modeler (83), with the lowest-energy predicted structure being chosen from 10 possible conformations. The positions of the rest of the heavy atoms of the side chains, except C_β, which is explicitly represented in AWSEM, were computed using SCWRL4 (84). The structures generated from this process were then visualized using PyMOL (85). The SASA values were estimated using a native function in PyMOL, in which a rolling a sphere with radius 1.4 Å, representing a water molecule, is used to race over the exposed atoms of the peptides and the fibril.

Data Availability. The datasets generated and analyzed during the current study are included in [SI Appendix](#). The computational methods used in this study were developed under the umbrella of our foundational AWSEM force field, deposited in the AWSEM web server (<https://awsem.rice.edu/>) and OpenAWSEM website (<https://openawsem.org/>) at Rice University, which is based off a GitHub code repository (<https://github.com/npschafer/openawsem>). The AWSEM code has been developed modularly over several years. We use line arguments and parameter files to adjust standard, codified procedures carried out by the functional scripts in our program.

ACKNOWLEDGMENTS. We thank C. Pennington for the liquid chromatography-mass spectroscopy characterization of the Aβ peptide and P. Cirino for access to facilities and advice on protein expression and purification. This work was supported by the NSF (Award No. DMR-1710354), NIH (Award No. AI150763), and the Center for Theoretical Biological Physics at Rice University sponsored by NSF (Award No. PHY-2019745). Additional support to P.G.W. was provided by the D.R. Bullard-Welch Chair at Rice University (Grant No. C-0016).

1. T. P. J. Knowles, M. Vendruscolo, C. M. Dobson, The amyloid state and its association with protein misfolding diseases. *Nat. Rev. Mol. Cell Biol.* **15**, 384–396 (2014).
2. A. Aguzzi, T. O'Connor, Protein aggregation diseases: Pathogenicity and therapeutic perspectives. *Nat. Rev. Drug Discov.* **9**, 237–248 (2010).
3. J. A. Hardy, G. A. Higgins, Alzheimer's disease: The amyloid cascade hypothesis. *Science* **256**, 184–185 (1992).
4. E. Levy et al., Mutation of the Alzheimer's disease amyloid gene in hereditary cerebral hemorrhage, Dutch type. *Science* **248**, 1124–1126 (1990).
5. Alzheimer's Association, 2021 Alzheimer's disease facts and figures. *Alzheimers Dement.* **17**, 327–406 (2021).
6. M.R. Brier, et al. Tau and Aβ imaging, CSF measures, and cognition in Alzheimer's disease. *Sci. Transl. Med.* **8**, 338ra366 (2016).
7. R. Nortley et al., Amyloid β oligomers constrict human capillaries in Alzheimer's disease via signaling to pericytes. *Science* **365**, eaav9518 (2019).
8. G. M. Shankar et al., Amyloid-β protein dimers isolated directly from Alzheimer's brains impair synaptic plasticity and memory. *Nat. Med.* **14**, 837–842 (2008).
9. R. Kaye et al., Common structure of soluble amyloid oligomers implies common mechanism of pathogenesis. *Science* **300**, 486–489 (2003).
10. G. Leinenga, J. Götz, Scanning ultrasound removes amyloid-β and restores memory in an Alzheimer's disease mouse model. *Sci. Transl. Med.* **7**, 278ra233 (2015).
11. J.-X. Lu et al., Molecular structure of β-amyloid fibrils in Alzheimer's disease brain tissue. *Cell* **154**, 1257–1268 (2013).
12. P. E. Cramer et al., ApoE-directed therapeutics rapidly clear β-amyloid and reverse deficits in AD mouse models. *Science* **335**, 1503–1506 (2012).

13. A. R. Price *et al.*, Comment on "ApoE-directed therapeutics rapidly clear β -amyloid and reverse deficits in AD mouse models". *Science* **340**, 924 (2013).
14. R. E. Uhlmann *et al.*, Acute targeting of pre-amyloid seeds in transgenic mice reduces Alzheimer-like pathology later in life. *Nat. Neurosci.* **23**, 1580–1588 (2020).
15. G. C. Alexander, S. Emerson, A. S. Kesselheim, Evaluation of aducanumab for Alzheimer disease: Scientific evidence and regulatory review involving efficacy, safety, and utility. *JAMA* **325**, 1717–1718 (2021).
16. P. K. Panda, A. S. Patil, P. Patel, H. Panchal, Mutation-based structural modification and dynamics study of amyloid beta peptide (1–42): An in-silico-based analysis to cognize the mechanism of aggregation. *Genom. Data* **7**, 189–194 (2016).
17. M. Takami *et al.*, γ -Secretase: Successive tripeptide and tetrapeptide release from the transmembrane domain of β -carboxyl terminal fragment. *J. Neurosci.* **29**, 13042–13052 (2009).
18. T. L. Kukar *et al.*, Lysine 624 of the amyloid precursor protein (APP) is a critical determinant of amyloid β peptide length: Support for a sequential model of γ -secretase intramembrane proteolysis and regulation by the amyloid β precursor protein (APP) juxtamembrane region. *J. Biol. Chem.* **286**, 39804–39812 (2011).
19. G. Bitan *et al.*, Amyloid β -protein (A β) assembly: A β 40 and A β 42 oligomerize through distinct pathways. *Proc. Natl. Acad. Sci. U.S.A.* **100**, 330–335 (2003).
20. J. T. Jarrett, P. T. Lansbury Jr, Seeding "one-dimensional crystallization" of amyloid: A pathogenic mechanism in Alzheimer's disease and scrapie? *Cell* **73**, 1055–1058 (1993).
21. S. A. Gravina *et al.*, Amyloid β protein (A β) in Alzheimer's disease brain. Biochemical and immunocytochemical analysis with antibodies specific for forms ending at A β 40 or A β 42(43). *J. Biol. Chem.* **270**, 7013–7016 (1995).
22. T. Iwatsubo *et al.*, Visualization of A β 42(43) and A β 40 in senile plaques with end-specific A β monoclonals: Evidence that an initially deposited species is A β 42(43). *Neuron* **13**, 45–53 (1994).
23. M. Kollmer *et al.*, Cryo-EM structure and polymorphism of A β amyloid fibrils purified from Alzheimer's brain tissue. *Nat. Commun.* **10**, 4760 (2019).
24. J. E. Straub, D. Thirumalai, Toward a molecular theory of early and late events in monomer to amyloid fibril formation. *Annu. Rev. Phys. Chem.* **62**, 437–463 (2011).
25. W. Zheng, M.-Y. Tsai, M. Chen, P. G. Wolynes, Exploring the aggregation free energy landscape of the amyloid- β protein (1–40). *Proc. Natl. Acad. Sci. U.S.A.* **113**, 11835–11840 (2016).
26. C.-T. Lee, E. M. Terentjev, Mechanisms and rates of nucleation of amyloid fibrils. *J. Chem. Phys.* **147**, 105103 (2017).
27. D. Kashchiv, S. Auer, Nucleation of amyloid fibrils. *J. Chem. Phys.* **132**, 215101 (2010).
28. T. C. T. Michaels *et al.*, Dynamics of oligomer populations formed during the aggregation of Alzheimer's A β 42 peptide. *Nat. Chem.* **12**, 445–451 (2020).
29. A. T. Petkova *et al.*, Self-propagating, molecular-level polymorphism in Alzheimer's β -amyloid fibrils. *Science* **307**, 262–265 (2005).
30. R. Tycko, Physical and structural basis for polymorphism in amyloid fibrils. *Protein Sci.* **23**, 1528–1539 (2014).
31. W. Qiang, K. Kelley, R. Tycko, Polymorph-specific kinetics and thermodynamics of β -amyloid fibril growth. *J. Am. Chem. Soc.* **135**, 6860–6871 (2013).
32. T. P. J. Knowles *et al.*, An analytical solution to the kinetics of breakable filament assembly. *Science* **326**, 1533–1537 (2009).
33. M. Törnquist *et al.*, Secondary nucleation in amyloid formation. *Chem. Commun. (Camb.)* **54**, 8667–8684 (2018).
34. I. W. Hamley, The amyloid beta peptide: A chemist's perspective. Role in Alzheimer's and fibrillization. *Chem. Rev.* **112**, 5147–5192 (2012).
35. S. I. A. Cohen *et al.*, Distinct thermodynamic signatures of oligomer generation in the aggregation of the amyloid- β peptide. *Nat. Chem.* **10**, 523–531 (2018).
36. M. Biancalana, S. Koide, Molecular mechanism of Thioflavin-T binding to amyloid fibrils. *Biochim. Biophys. Acta* **1804**, 1405–1412 (2010).
37. M. S. Z. Kellermayer, A. Karsai, M. Benke, K. Soós, B. Penke, Stepwise dynamics of epitaxially growing single amyloid fibrils. *Proc. Natl. Acad. Sci. U.S.A.* **105**, 141–144 (2008).
38. Q. Huang *et al.*, In situ observation of amyloid nucleation and fibrillation by FastScan atomic force microscopy. *J. Phys. Chem. Lett.* **10**, 214–222 (2019).
39. M. Sleutel *et al.*, Nucleation and growth of a bacterial functional amyloid at single-fiber resolution. *Nat. Chem. Biol.* **13**, 902–908 (2017).
40. C. Goldsberry, J. Kistler, U. Aebi, T. Arvinte, G. J. S. Cooper, Watching amyloid fibrils grow by time-lapse atomic force microscopy. *J. Mol. Biol.* **285**, 33–39 (1999).
41. H. K. L. Blackley *et al.*, In-situ atomic force microscopy study of β -amyloid fibrillization. *J. Mol. Biol.* **298**, 833–840 (2000).
42. W. Hoyer, D. Cherny, V. Subramaniam, T. M. Jovin, Rapid self-assembly of α -synuclein observed by in situ atomic force microscopy. *J. Mol. Biol.* **340**, 127–139 (2004).
43. S. Banerjee, M. Hashemi, K. Zagorski, Y. L. Lyubchenko, Interaction of A β 42 with membranes triggers the self-assembly into oligomers. *Int. J. Mol. Sci.* **21**, 1129 (2020).
44. S. Banerjee *et al.*, A novel pathway for amyloids self-assembly in aggregates at nanomolar concentration mediated by the interaction with surfaces. *Sci. Rep.* **7**, 45592 (2017).
45. T. Ban, D. Hamada, K. Hasegawa, H. Naiki, Y. Goto, Direct observation of amyloid fibril growth monitored by thioflavin T fluorescence. *J. Biol. Chem.* **278**, 16462–16465 (2003).
46. D. Pinotti *et al.*, Direct observation of heterogeneous amyloid fibril growth kinetics via two-color super-resolution microscopy. *Nano Lett.* **14**, 339–345 (2014).
47. M. M. Würdehoff *et al.*, Single fibril growth kinetics of α -synuclein. *J. Mol. Biol.* **427**, 1428–1435 (2015).
48. S. M. Patil, A. Mehta, S. Jha, A. T. Alexandrescu, Heterogeneous amylin fibril growth mechanisms imaged by total internal reflection fluorescence microscopy. *Biochemistry* **50**, 2808–2819 (2011).
49. J. Ferkinghoff-Borg *et al.*, Stop-and-go kinetics in amyloid fibrillation. *Phys. Rev. E Stat. Nonlin. Soft Matter Phys.* **82**, 010901 (2010).
50. Y. Xu *et al.*, Steady, symmetric, and reversible growth and dissolution of individual amyloid- β fibrils. *ACS Chem. Neurosci.* **10**, 2967–2976 (2019).
51. T. Watanabe-Nakayama, B. R. Sahoo, A. Ramamoorthy, K. Ono, High-speed atomic force microscopy reveals the structural dynamics of the amyloid- β and amylin aggregation pathways. *Int. J. Mol. Sci.* **21**, 4287 (2020).
52. Y.-C. Lin, C. Li, Z. Fakhraei, Kinetics of surface-mediated fibrillization of amyloid- β (12–28) peptides. *Langmuir* **34**, 4665–4672 (2018).
53. L. Hua, R. Zhou, D. Thirumalai, B. J. Berne, Urea denaturation by stronger dispersion interactions with proteins than water implies a 2-stage unfolding. *Proc. Natl. Acad. Sci. U.S.A.* **105**, 16928–16933 (2008).
54. M. Auton, L. M. F. Holthausen, D. W. Bolen, Anatomy of energetic changes accompanying urea-induced protein denaturation. *Proc. Natl. Acad. Sci. U.S.A.* **104**, 15317–15322 (2007).
55. J.R. Kim, A. Muresan, K.Y.C. Lee, R.M. Murphy, Urea modulation of beta-amyloid fibril growth: Experimental studies and kinetic models. *Protein Sci.* **13**, 2888–2898 (2004).
56. C. L. Berthollet, *Essai De Statique Chimique; Premiere Partie* (Demonville et Soers, Paris, 1803).
57. S. Zambelli, "Chemical kinetics, an historical introduction" in *Chemical Kinetics*, V. Patel, Ed. (InTech Rijeka, Croatia, 2012), pp. 3–28.
58. M. Warzecha *et al.*, Olanzapine crystal symmetry originates in preformed centrosymmetric solute dimers. *Nat. Chem.* **12**, 914–920 (2020).
59. J. P. Cleary *et al.*, Natural oligomers of the amyloid- β protein specifically disrupt cognitive function. *Nat. Neurosci.* **8**, 79–84 (2005).
60. B. Tarus *et al.*, Structures of the Alzheimer's wild-type A β 1–40 dimer from atomistic simulations. *J. Phys. Chem. B* **119**, 10478–10487 (2015).
61. W. Qiang, W.-M. Yau, J.-X. Lu, J. Collinge, R. Tycko, Structural variation in amyloid- β fibrils from Alzheimer's disease clinical subtypes. *Nature* **541**, 217–221 (2017).
62. J. C. Stroud, C. Liu, P. K. Teng, D. Eisenberg, Toxic fibrillar oligomers of amyloid- β have cross- β structure. *Proc. Natl. Acad. Sci. U.S.A.* **109**, 7717–7722 (2012).
63. A. W. P. Fitzpatrick *et al.*, Atomic structure and hierarchical assembly of a cross- β amyloid fibril. *Proc. Natl. Acad. Sci. U.S.A.* **110**, 5468–5473 (2013).
64. A. K. Paravastu, R. D. Leapman, W.-M. Yau, R. Tycko, Molecular structural basis for polymorphism in Alzheimer's β -amyloid fibrils. *Proc. Natl. Acad. Sci. U.S.A.* **105**, 18349–18354 (2008).
65. N. Schwier, C. V. Frost, P. L. Geissler, M. Zacharias, Dynamics of seeded A β 40-fibril growth from atomistic molecular dynamics simulations: Kinetic trapping and reduced water mobility in the locking step. *J. Am. Chem. Soc.* **138**, 527–539 (2016).
66. K. Kawahara, C. Tanford, Viscosity and density of aqueous solutions of urea and guanidine hydrochloride. *J. Biol. Chem.* **241**, 3228–3232 (1966).
67. M. Oliveberg, P. G. Wolynes, The experimental survey of protein-folding energy landscapes. *Q. Rev. Biophys.* **38**, 245–288 (2005).
68. H. J. Bakker, J. L. Skinner, Vibrational spectroscopy as a probe of structure and dynamics in liquid water. *Chem. Rev.* **110**, 1498–1517 (2010).
69. E. S. Courtenay, M. W. Capp, M. T. Record Jr, Thermodynamics of interactions of urea and guanidinium salts with protein surface: Relationship between solute effects on protein processes and changes in water-accessible surface area. *Protein Sci.* **10**, 2485–2497 (2001).
70. J. D. Bryngelson, P. G. Wolynes, Spin glasses and the statistical mechanics of protein folding. *Proc. Natl. Acad. Sci. U.S.A.* **84**, 7524–7528 (1987).
71. J. N. Onuchic, N. D. Socci, Z. Luthey-Schulten, P. G. Wolynes, Protein folding funnels: The nature of the transition state ensemble. *Fold. Des.* **1**, 441–450 (1996).
72. M. Chen *et al.*, Surveying biomolecular frustration at atomic resolution. *Nat. Commun.* **11**, 5944 (2020).
73. M. Chen, P. G. Wolynes, Aggregation landscapes of Huntingtin exon 1 protein fragments and the critical repeat length for the onset of Huntington's disease. *Proc. Natl. Acad. Sci. U.S.A.* **114**, 4406–4411 (2017).
74. M. Chen, N. P. Schaefer, P. G. Wolynes, Surveying the energy landscapes of A β fibril polymorphism. *J. Phys. Chem. B* **122**, 11414–11430 (2018).
75. W. P. Esler *et al.*, Alzheimer's disease amyloid propagation by a template-dependent dock-lock mechanism. *Biochemistry* **39**, 6288–6295 (2000).
76. T. Gurry, C. M. Stultz, Mechanism of amyloid- β fibril elongation. *Biochemistry* **53**, 6981–6991 (2014).
77. J. K. Myers, C. N. Pace, J. M. Scholtz, Denaturant m values and heat capacity changes: Relation to changes in accessible surface areas of protein unfolding. *Protein Sci.* **4**, 2138–2148 (1995).
78. A. Davtyan *et al.*, AWSEM-MD: Protein structure prediction using coarse-grained physical potentials and bioinformatically based local structure biasing. *J. Phys. Chem. B* **116**, 8494–8503 (2012).
79. D. M. Walsh *et al.*, A facile method for expression and purification of the Alzheimer's disease-associated amyloid beta-peptide. *FEBS J.* **276**, 1266–1281 (2009).
80. G. Tesei *et al.*, Aggregate size dependence of amyloid adsorption onto charged interfaces. *Langmuir* **34**, 1266–1273 (2018).
81. A. T. Petkova, W.-M. Yau, R. Tycko, Experimental constraints on quaternary structure in Alzheimer's β -amyloid fibrils. *Biochemistry* **45**, 498–512 (2006).
82. M. R. Shirts, J. D. Chodera, Statistically optimal analysis of samples from multiple equilibrium states. *J. Chem. Phys.* **129**, 124105 (2008).
83. B. Webb, A. Sali, Comparative protein structure modeling using modeller. *Curr. Protoc. Bioinformatics* **54**, 5.6.1–5.6.37 (2016).
84. G. G. Krivov, M. V. Shapovalov, R. L. Dunbrack Jr, Improved prediction of protein side-chain conformations with SCWRL4. *Proteins* **77**, 778–795 (2009).
85. W.L. DeLano, Pymol: An open-source molecular graphics tool. *CCP4 Newsletter Protein Crystallography* **40**, 82–92 (2002).